1   *A deep learning algorithm to translate and classify cardiac*

2   *electrophysiology: From induced pluripotent stem cell-derived*

3   *cardiomyocytes to adult cardiac cells*

4

5   Parya Aghasafari PhD[1], Pei-Chi Yang PhD[1], Divya C. Kernik PhD[2], Kauho Sakamoto PhD[4], Yasunari

6   Kanda PhD[5], Junko Kurokawa PhD[4], Igor Vorobyov PhD[1,6] and Colleen E. Clancy PhD[1,3]

7

8   [1] Department of Physiology and Membrane Biology
9   University of California Davis, Davis, CA
10
11   [2] Washington University in St. Louis
12
13   [4]Department of Bio-Informational Pharmacology
14   School of Pharmaceutical Sciences
15   University of Shizuoka
16   Shizuoka, Japan
17
18   [5]Division of Pharmacology
19   National Institute of Health Sciences
20   Kanagawa, Japan
21
22   [6]Department of Pharmacology
23   University of California, Davis, CA
24
25   [3] Correspondence: Colleen E. Clancy, Ph.D.
26   University of California, Davis
27   Tupper Hall, RM 4303
28   Davis, CA 95616-8636
29   Email: ceclancy@ucdavis.edu
30
31   Phone: 530-754-0254
32   Word count:
33   Subject code: Artificial Intelligence, Machine Learning, Deep Learning, Computational Biology,
34   Arrhythmias, Pharmacology.
35   Short title: Translation of cardiac action potential from immature to mature

36   Abstract

37   The development of induced pluripotent stem cell-derived cardiomyocytes (iPSC-CMs) has been a

38   critical in vitro advance in the study of patient-specific physiology, pathophysiology and

39   pharmacology. We designed a new deep learning multitask network approach intended to address

40   the low throughput, high variability and immature phenotype of the iPSC-CM platform. It was

41   trained using simulated action potential (AP) data and applied to classify cells into the drug-free

42   and drugged categories and to predict the impact of electrophysiological perturbation across the

43   continuum of aging from the immature iPSC-CMs to the adult ventricular myocytes. The phase of

44   the AP extremely sensitive to perturbation due to a steep rise of the membrane resistance was

45   found to contain the key information required for successful network multitasking. We also

46   demonstrated successful translation of both experimental and simulated iPSC-CM AP data

47   validating our network by prediction of experimental drug-induced effects on adult cardiomyocyte

48   APs by the latter.

49 Introduction

50 The development of novel technologies has resulted in new ways to study cardiac function and

51 rhythm disorders [1]. One such technology is the induced pluripotent stem cell-derived

52 cardiomyocyte (iPSC-CMs) *in vitro* model system [2]. The iPSC-CM system constitutes a powerful

53 *in vitro* tool for preclinical assessment of cardiac electrophysiological impact and drug safety

54 liabilities in a human physiological context [3-8]. Moreover, because iPSC-CMs can be cultured

55 from patient specific-cells, it has shown to be an ideal model system for patient-based medicine

56 [8-10].

57

58 While utilization of *in vitro* iPSC-CMs allows for testing of responses to drugs and understanding

59 physiological mechanisms [11-14], there is still a major inherent limitation of the approach: The

60 complex differentiation process to create iPSC-CMs results in a model of cardiac electrical behavior

61 that resembles fetal cardiomyocytes. Hallmarks of the immature phenotype include spontaneous

62 beating, immature calcium handling, presence of developmental currents, and significant

63 differences in the relative contributions of repolarizing potassium currents compared to adult

64 cardiomyocytes (adult-CMs) [15-17]. The profound differences between the immature iPSC-CMs

65 and the adult-CMs have led to persistent questions about the utility and applicability of the iPSC-

66 CM action potential (AP) to predict relevant drug impacts on adult human electrophysiology [18,

67 19].

68

69 Several recent studies have proposed computational frameworks to address the primary limitation

70 in using iPSC-CMs and animal cardiomyocytes for drug screening [11, 12, 20, 21]. The innovative

71 studies described by Tvieto and colleagues [9, 10] presented a translation algorithm that identified

72 a mapping function to identify the relationships between the parameters that are defined by key

73 ion channel conductances in the iPSC-CM APs and the adult-CM APs. In another study by Gong

74 and Sobie, additional insights were revealed through application of an efficient partial least

75 squares regression (PLSR) methodology to translate key physiological features between iPSC-CMs

76 and adult-CMs. They also demonstrated the potential to translate between species, between drug-

77 free and simple drugged models as well as between healthy and diseased phenotypes [20].

78   Koivumäki et al. also tried to address the problem of iPSC-CMs immaturity by establishing a novel

79   *in silico* mathematical model for iPSC-CMs, which can estimate adult-CM behavior [22].

80

81   The efficacy of the linear translation algorithms used in the earlier studies relies on a collection of

82   underlying assumptions [20]. One described by Tvieto et al. is that cardiac protein expression levels

83   would differ but their functional properties remain invariant during maturation and that a drug

84   will modify protein function in the same way for iPSC-CMs and the adult-CMs [11]. Tvieto et al.

85   also acknowledged the difficulty in minimizing the cost function that measures the differences

86   between the initial and target parameters, which therefore required a brute force search

87   algorithm for minimization. One possible explanation for the difficulty in cost function

88   minimization is that linear translation may not capture the nonlinearities comprising the actual

89   underlying physiological differences [20]. Another underlying assumption with linear translation is

90   the required representation of drug effects as a simple pore-block, modeled as a reduction in the

91   maximal conductance of the channel [11, 20]. The earlier studies employed a biased method in

92   that they rely on *a priori* parameter identification and extraction from voltage and calcium traces

93   to allow feature mapping from immature to mature conditions [11, 20]. Earlier translators must

94   also consider drug-free and drugged conditions independently.

95

96   In this study, we describe a deep learning multitask network that simultaneously performs

97   translation and classification of signals from simulated cardiac myocytes for both drug-free and

98   drugged conditions and we demonstrate its utility for translating and predicting experimental data

99   as well. The multitask network is an unbiased approach in that the user does not predefine the

100   important parameters of the system. Rather, the network learns from the data to define important

101   parameter regimes and data ranges. The new approach is indifferent to the underlying form of the

102   models and can translate time series data from any source. Moreover, the deep learning approach

103   accepts non-linearity of the system, makes no assumptions about changes in cardiac protein

104   expression and function during maturation and can successfully translate simple pore block and

105   complex conformation state-dependent channel – drug interaction. The network learns from all

106   of these data sources for robust and successful translation, suggesting broad applicability.

4

107   Artificial neural networks are increasingly used to advance personalized medicine [23-27]. Long-

108   short-term-memory (LSTM) based networks, which are capable of learning order dependence in

109   sequence prediction problems [28], have been widely used for cardiac monitoring purposes [29-

110   31]. They have been used to extract important biomarkers from raw ECG signals [32-34] and help

111   clinicians to accurately detect common heart failure biomarkers in ECG screenings [32, 35-39].

112   LSTM networks, which can catch existing temporal information in the electronic health records

113   (EHR), have been highlighted as the best predictive models using real time data [40]. LSTM based

114   classifiers have also empowered early arrhythmia detection by automatically classifying

115   arrhythmias using ECG features [41-45]. In addition, deep learning algorithms have been employed

116   to predict drug-induced arrhythmogenicity associated with blockade of the delayed rectifier K$^+$

117   channel current (I_{Kr}) in the CMs encoded by human ether-à-go-go-related gene (hERG) [46] for

118   sets of small molecules in drug discovery and screening process [46-51].

119

120   Here, we implemented a deep learning LSTM based multitask network to classify iPSC-CM AP

121   traces into drug-free and drugged categories and translate them into adult-CM AP waveforms. To

122   collect robust realistic simulated data for training the multitask network, we paced simulated

123   cardiac myocytes with the addition of a physiological noise current at matching cycle lengths for

124   Kernik *in silico* iPSC-CMs [52] and O'Hara-Rudy *in silico* human adult-CMs [53] to generate a

125   population of drug-free simulated cardiac myocyte data. To ensure that our model could perform

126   for both drug-free and drugged iPSC-CM and adult-CM APs simultaneously, we simulated drugged

127   samples via both a simple drug-induced I_{Kr} block model of hERG channel conduction, G_{Kr}, reduction

128   by *1-50%* and a complex Markov model of conformation-state dependent I_{Kr} block in the presence

129   of a clinical concentration, *2.72 ng/mL*, of a potent hERG blocking drug dofetilide from our recent

130   study [46]. We evaluated the multitask network performance on a test dataset and showed

131   excellent performance to translate and classify signals in the form of time-resolved AP traces. We

132   performed an ablation study to reveal the most important iPSC-CM AP information for network

133   translation into adult-CM APs by removing iPSC-CM AP values during various time frames (feature

134   ablation). We also explored the importance of individual LSTM network building blocks and how

135   decoupling of the translation and classification tasks affected overall network performance. We

5

136   then showed how proposed multitask network can be applied even to scarce experimental data,

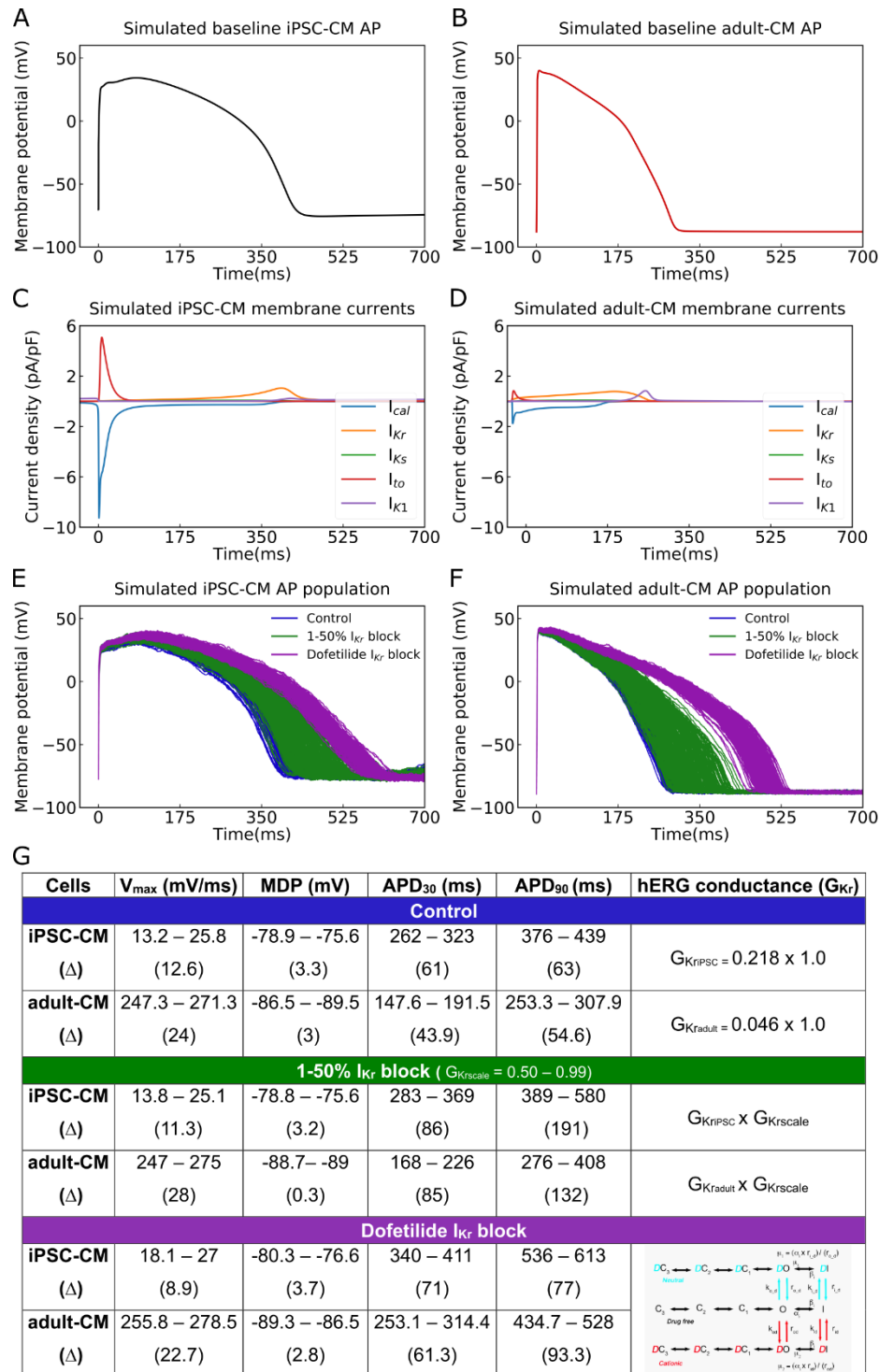137   which was also used to validate the model.

138

139   In this study we show that developments in iPSC-CM experimental technology and cardiac

140   electrophysiological modeling and simulation of iPSC-CMs can be leveraged for the application of

141   artificial neural networks (ANN) as a universal approximator [54] to find the most accurate

142   mapping function which is capable of learning nonlinear relationships to predict disease

143   phenotype and drug response in cardiac myocytes from immaturity to maturation.

144

145   Results

146   In this study, we set out to build a multitask network that would perform two distinct tasks: The

147   first task is to classify iPSC-CM APs into drug-free and drugged categories. The second goal is to

148   translate iPSC-CM APs into corresponding adult-CM AP waveforms. To collect the data for training

149   the multitask network, we simulated a population of 208 AP waveforms for both Kernik *in silico*

150   human iPSC-CMs [52] (Figure 1E blue) and O'Hara-Rudy *in silico* human adult-CMs [53] (Figure 1F

151   blue). We ensured consistency across a population of simulated myocytes by applying

152   physiological noise at the matching the cycle lengths into the iPSC-CMs and adult-CMs. The cell

153   variability in each population is intended to represent the individual variability that is observed in

154   a drug-free human population [52, 53, 55]. An average AP trace from the population is shown in

155   Figure 1A for iPSC-CMs and Figure 1B for adult-CMs. In Figure 1 panels C and D, the ionic currents

156   underlying the *in silico* iPSC-CM APs and adult-CM APs show marked differences, one reason for

157   the broadly expressed concerns about the applicability of utilizing immature iPSC-CM APs in the

158   study of human disease and pharmacology. The substantial current differences illustrate the

159   necessity of a generalized approach to perform translation from immature myocytes into mature

160   myocytes. To ensure that our multitask network could perform over a range of conditions and

161   model forms, we simulated drugged iPSC-CM and adult-CM APs via both a simple I_{Kr} drug block

162   model of G_{Kr} reduction by *1-50%* (250 samples in Figure 1E, F green) and a complex model of

163   conformation-state dependent I_{Kr} block in the presence of *2.72 ng/mL* dofetilide (300 samples in

164   Figure 1E, F purple). We combined the drug-free and drugged models with simple and complex I_{Kr}

6

165   block model schemes (758 samples) for training the multitask network. The differences in key

166   parameters, upstroke velocity (V_{max}), maximum diastolic potential (MDP) and action potential

167   durations (APD) across the three conditions are tabulated and shown in Figure 1G.

Cells	V_{max} (mV/ms)	MDP (mV)	APD_{30} (ms)	APD_{90} (ms)	hERG conductance (G_{Kr})
Control					
iPSC-CM	13.2 – 25.8	-78.9 – -75.6	262 – 323	376 – 439	G_{KriPSC} = 0.218 x 1.0
(Δ)	(12.6)	(3.3)	(61)	(63)	
adult-CM	247.3 – 271.3	-86.5 – -89.5	147.6 – 191.5	253.3 – 307.9	$G_{Kradult}$ = 0.046 x 1.0
(Δ)	(24)	(3)	(43.9)	(54.6)	
1-50% I_{Kr} block ($G_{Krscale}$ = 0.50 – 0.99)					
iPSC-CM	13.8 – 25.1	-78.8 – -75.6	283 – 369	389 – 580	G_{KriPSC} x $G_{Krscale}$
(Δ)	(11.3)	(3.2)	(86)	(191)	
adult-CM	247 – 275	-88.7 – -89	168 – 226	276 – 408	$G_{Kradult}$ x $G_{Krscale}$
(Δ)	(28)	(0.3)	(85)	(132)	
Dofetilide I_{Kr} block					
iPSC-CM	18.1 – 27	-80.3 – -76.6	340 – 411	536 – 613	
(Δ)	(8.9)	(3.7)	(71)	(77)	
adult-CM	255.8 – 278.5	-89.3 – -86.5	253.1 – 314.4	434.7 – 528	
(Δ)	(22.7)	(2.8)	(61.3)	(93.3)	

Figure 1. Cellular action potential (AP) and ionic currents for iPSC-CMs and adult-CMs (O'Hara-Rudy human ventricular action potentials). Comparison of Cellular APs in the baseline model of (A) iPSC-CMs and (B) adult-CMs at a matched cycle length of 982 ms. (C – D) Simulated ionic current (I_{CaL}, I_{Kr}, I_{Ks}, I_{to}, I_{K1}) profiles during (C) iPSC-CM and (D) adult-CM APs. (E) APs of

8

172   spontaneously beating iPSC-CM cells (n =208) and (F) adult-CM APs at matched cycle lengths

173   were simulated after incorporating physiological noise currents as drug-free (blue) and drugged

174   I_{Kr} modeled as simple G_{Kr} reduction by *1-50% I_{Kr}* block (green) and a complex model of

175   conformation-state dependent I_{Kr} block in the presence of *2.72 ng/mL* dofetilide (purple). (G)

176   Comparison between iPSC-CM and adult-CM drug-free and drugged models with simple and

177   complex I_{Kr} block model schemes (as indicated in right column), including upstroke velocity

178   (V_{max}), maximum diastolic potential (MDP) and action potential duration (APD).

179

180   Next, we applied a digital forward and backward data filtering technique [56] to the simulated

181   iPSC-CM and adult-CM AP traces (Figure 2 left panels). Since we applied physiological noise to

182   introduce a source of variability (as observed in human populations) in our model simulations, we

183   assessed the possible phase distortion for AP waveforms following noise filtering. In Figure 2 (right

184   panels), the distribution of iPSC-CM and adult-CM AP duration at 90% repolarization (APD_{90}) values

185   are shown. The near superimposition of the histogram distributions assures that noise filtering

186   does not change the AP waveform morphology or time course and primarily removes existing

187   vertical noises. Panel A and B show simulated drug-free iPSC-CM and adult-CM APs and

188   corresponding APD_{90} distribution with physiological noise in blue and after applying the noise

189   filtering technique in black for iPSC-CM APs and red for adult-CM APs. The same plots are

190   illustrated for drugged AP traces with simple *1-50% I_{Kr}* block (Figure 2C and D) and with complex

191   I_{Kr} block model in the presence of *2.72 ng/mL* dofetilide (Figure 2E and F). Next, we normalized

192   drug-free and drugged noise-filtered iPSC-CM APs and adult-CM APs to use them as input and

193   output, respectively, for training the multitask network.

9
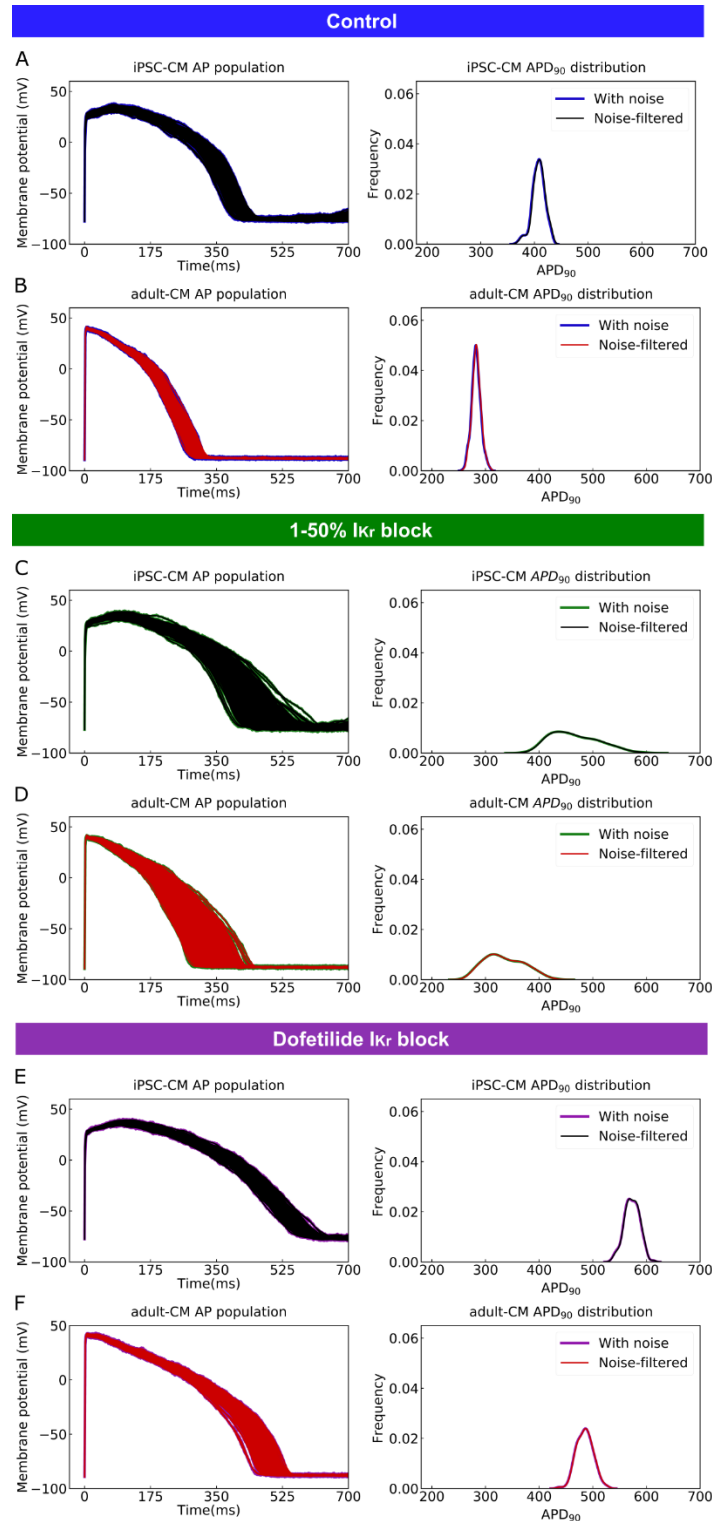
Figure 2. Application of a digital forward and backward data filtering technique to simulated iPSC-CM and adult-CM APs population (left panels) indicates zero phase distortion for APD_{90} value distributions (right panels) for: (A) drug-free iPSC-CM APs with physiological noise in blue and after applying the noise filtering technique in black; (B) drug-free adult-CM APs – blue and red traces; (C) drugged iPSC-CM APs with *1-50% I_{Kr}* block – green and black traces; (D) drugged

10

199   adult-CM APs with *1-50% I_{Kr}* block – green and red traces; (E) drugged iPSC-CM APs with *2.72*
200   *ng/mL* dofetilide – purple and black traces. (F) drugged adult-CM APs with *2.72 ng/mL* dofetilide
201   –purple and red traces.

202   The building blocks of the multitask network are illustrated in Figure 3A. The multitask network

203   receives preprocessed simulation generated iPSC-CM AP waveforms (noise-filtered and

204   normalized) as input and scans whole AP time series values through two stacked LSTM layers

205   (Figure 3A, D). The LSTM layers remember the most important iPSC-CM AP values (features) they

206   need to perform the translation and classification tasks and passes the information to two fully

207   connected layers (Figure 3A, E), one for the translation task to predict the corresponding adult-

208   CM AP waveform (Figure 3B) and one for the classification task to classify iPSC-CM APs into drug-

209   free and drugged categories (Figure 3C).

210
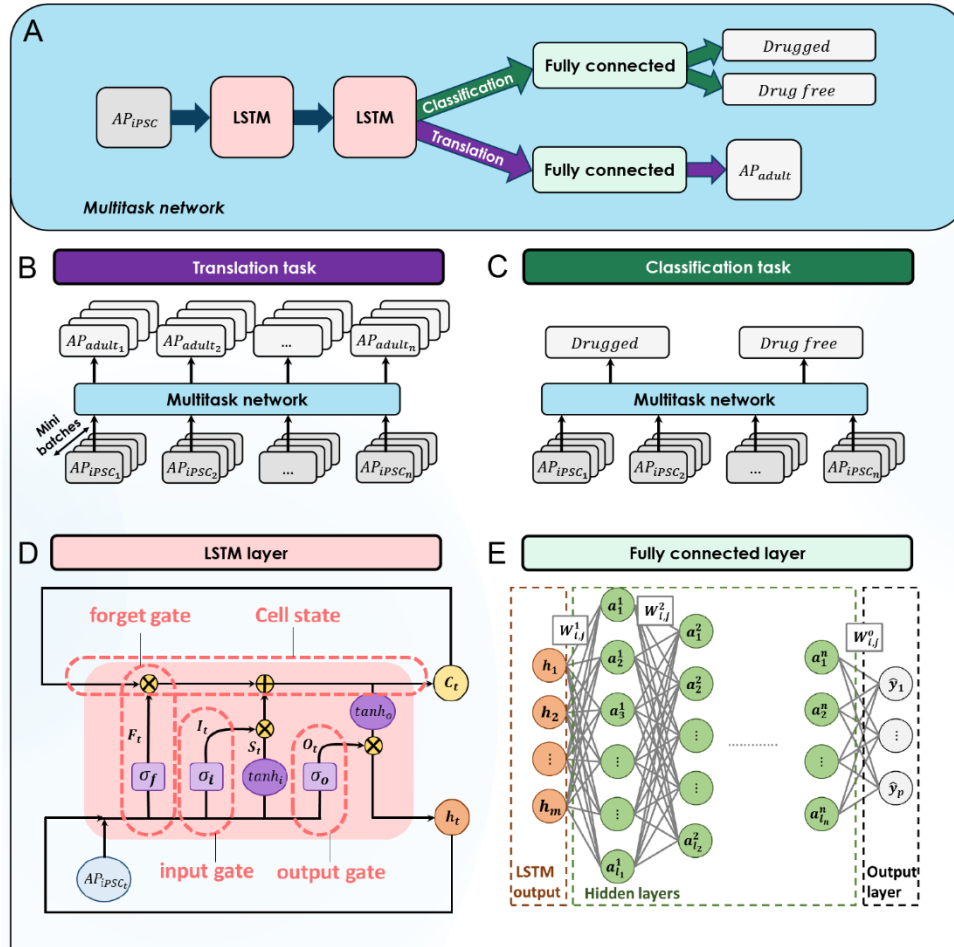
11

Figure 3. The building blocks of the multitask network. (A) The general overview of the multitask network presented in this study. (B) The translation task to reconstruct adult-CM APs from corresponding iPSC-CM APs. (C) The classification task to classify iPSC-CM APs into drug-free and drugged categories. (D) The logic flow process in the LSTM layers. (E) The architecture of the implemented fully connected layers in the multitask network.

The workflow for training and evaluating the multitask network is depicted in Figure 4. As described above, we generated simulated drug-free and drugged iPSC-CM and adult-CM APs and applied a noise filtering technique to the AP waveforms. The waveforms were then normalized in a data preprocessing step for more efficient training of the multitask network. We used preprocessed iPSC-CM APs as the network input and adult-CM APs along with corresponding drug-free and drugged labels as network outputs, respectively. Next, we randomly split input and output data in 70:10:20 ratio into three subcategories: training, validation, and test data sets. We used the training dataset for training the multitask network to simultaneously perform translation and

12

225 classification. The mean squared error, R^2-score [57] and error in adult-CM APD_{90} prediction were

226 used as evaluation metrics for the translation task. For the classification task, area under the

227 receiver operating characteristic (AUROC) curve [58], network prediction accuracy, precision and

228 recall [59] were used to evaluate the network performance. To prevent overfitting, we calculated

229 the evaluation metrics for both tasks using validation data during each iteration of training and

230 compared those with values from the training dataset. When the model performance on the

231 training dataset exhibited degradation relative to the validation dataset, we ceased training and

232 tuning of the network hyperparameters. We evaluated the underlying mechanisms that inform

233 the network performance by using a holdout test data set to perform an ablation study. The

234 ablation study allowed us to identify the most important information for network performance

235 and is an indicator of the data that the network deems most important to remember to allow

236 accurate translation into adult-CM APs (feature ablation). Finally, we performed a type of network

237 component dissection by sequentially eliminating individual LSTM layers or the classification task

238 to determine if all elements of the network are important to the overall performance.

13
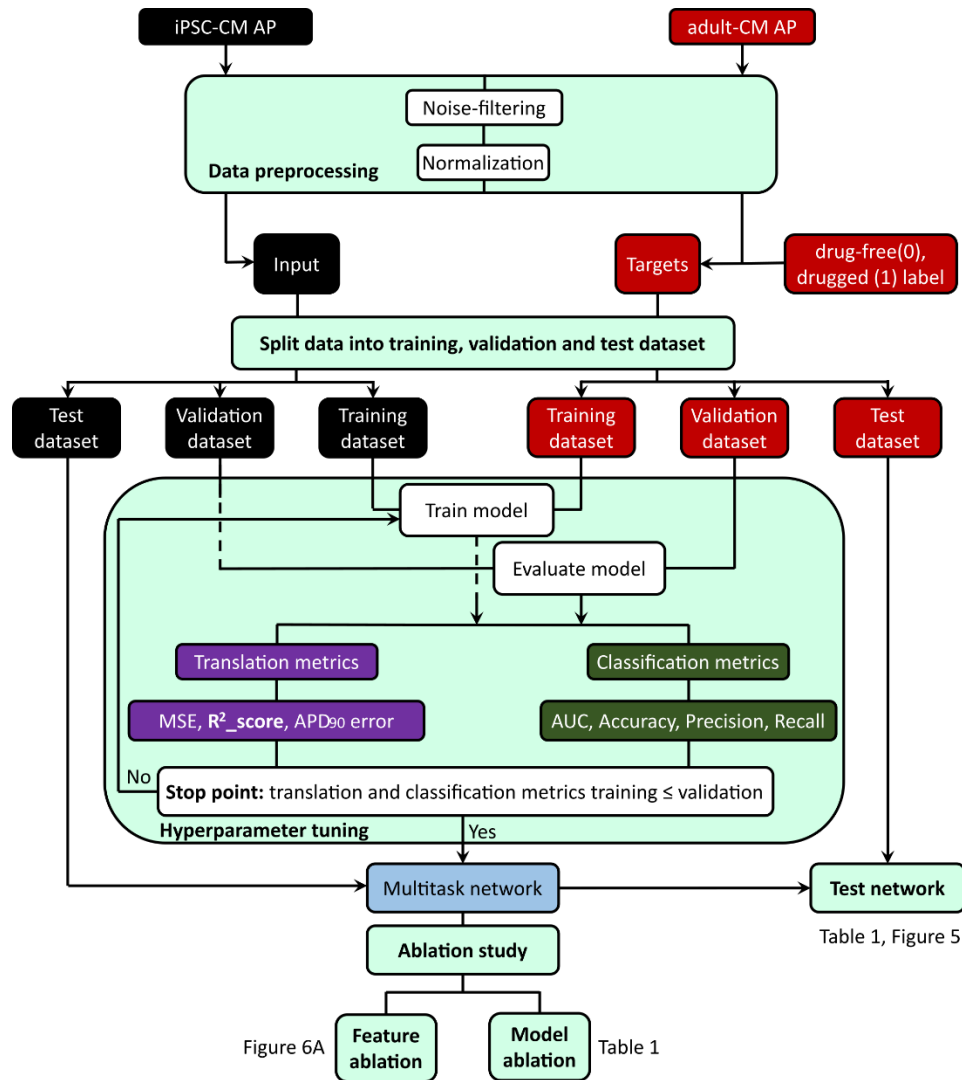
239   **Figure 4.** Machine learning workflow in this study: 1) Data preprocessing includes noise-filtering
240   and normalization of the drug-free and drugged iPSC-CM and adult-CM APs; 2) Incorporating the
241   preprocessed iPSC-CM APs as input and adult-CM APs and corresponding labels (drug-free (0)
242   and drugged (1)) of iPSC-CM APs as targets into the multitask network; 3) Splitting the input and
243   target data into training, validation and test set, and using training and validation set for training
244   and tuning the network hyperparameters; 4) Comparing the network performance for training
245   set and validation set to decide when to stop training and tuning the network hyperparameters;
246   5) Testing the overall multitask network performance using holdout test dataset and removing
247   the LSTM layers, classification task (model ablation) and iPSC-CM AP values at different time
248   frames (feature ablation) to study the performance of the network in the absence of its building
249   blocks.

250   Figure 5 and Table 1 illustrate the overall multitask network performance for translation and

251   classification tasks for the training and test data sets. Panels A and D in Figure 5 represent iPSC-

252   CM APs (black), which were used for training and testing the multitask network, respectively.

14

253   Panels B and E depict the comparison between simulated (red) and translated (cyan) adult-CM APs

254   used for the training and testing the network. The comparison between histogram distribution of

255   APD_{90} values for simulated and translated adult-CM APs in Figure 5C and F show good agreement

256   in terms of the frequency of virtual cells with similar APD.

257
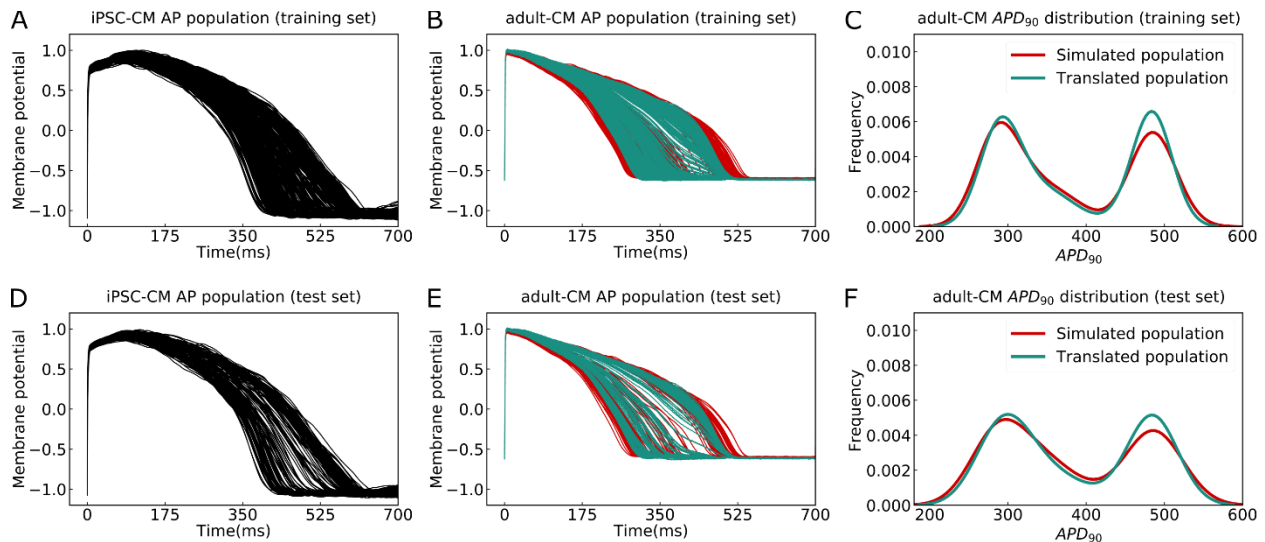
258

259   **Figure 5.** The performance of the multitask network for translating iPSC-CM APs into adult-CM
260   APs. (A) The iPSC-CM APs used for training the multitask network contained a variety of drug-
261   free and drugged action potential morphologies (Training set). (B) Comparison between
262   simulated (red) and translated adult-CM APs (cyan) in the training set. (C) Comparison between
263   the histogram distribution of APD_{90} values for simulated and translated adult-CM APs in the
264   training set. (D) Dedicated iPSC-CM APs for testing the performance of the multitask network
265   (Test set) (E) Comparison between simulated (red) and translated adult-CM APs (cyan) in the test
266   set. (F) Comparison between histogram distribution of APD_{90} values for simulated and translated
267   adult-CM APs in the test set.

268

269   The performance evaluation metrics for both the translation and classification tasks are listed in

270   Table 1. The multitask network exhibits high accuracy in performing translation, despite large

271   variability in APDs and regardless of the underlying model form. The network is able to translate

272   iPSC-CM APs into adult-CM APs with less than *0.003* mean-squared error (MSE), *0.99* R^2_score and

273   less than *4%* error in APD_{90} prediction for both training and test datasets. To evaluate the network

274   performance for the classification task we compared the AUROC, prediction accuracy, recall and

275   precision for both training and test datasets. The multitask network proved to perform well in

276   categorizing iPSC-CM APs into drug-free and drugged waveforms with approximately *90%*

15

277 accuracy (Table 1). Finally, we performed a type of network component dissection by sequentially

278 eliminating individual LSTM layers or the classification task to determine if all elements of the

279 network are important to the overall performance. The impact of removing these elements of the

280 network on the network performance is shown in Table 1.

281

282 **Table 1.** Statistical measures for evaluating the performance of the multitask network for both
283 iPSC-CM AP trace classification into drug-free and drugged categories and their translation into
284 adult-CM APs for training and test datasets as well as the effect of removing LSTM layers and
285 classification task on the network performance.

Translation			
Performance metrics	MSE	R^2_score	Error in APD_{90} prediction
Training dataset	0.0027	0.992	3.41%
Test dataset	0.0029	0.991	3.60%
Remove LSTM layers test dataset	0.0031	0.991	3.78%
Remove classification task test dataset	0.0034	0.990	4.33%

Classification				
Performance metrics	AUROC	Accuracy	Recall	Precision
Training dataset	0.93	92%	0.92	0.93
Test dataset	0.91	92%	0.92	0.92
Remove LSTM layers test dataset	0.90	92%	0.90	0.91

286 Next, we performed a "computational" ablation study as a correlate to the types of physiological

287 ablations that are used to examine the roles and functions of a physiological system [60, 61]. We

288 tested how the performance of the multitask network would change by removing various

289 information contained within specified time frames as shown in Figure 6A. To reveal the most

290 important iPSC-CM AP information for translation into adult-CM APs, we did not allow the network

291 to process data from within designated time frames from the iPSC-CM APs (feature ablation). We

292 then retrained the multitask network by setting the missing information equal to zero and

293 compared the calculated MSE in adult-CM APs translation (red bars) with the recorded MSE for

294 multitask network (green line) when it was provided full access to the complete iPSC-CM AP data.

295 We observed that network is extremely sensitive to information contained within the *400-500 ms*

296 timeframe (blacked dashed bar in Figure 6A).

297

16

298   This result suggests that the most important information needed to distinguish adult-CM AP

299   signals from iPSC-CM AP signals is contained in a particular region of the AP plateau. The

300   timeframe of the AP between 400 and 500 ms (Figure 6A), corresponds to a phase of exquisite

301   sensitivity to perturbation. We have identified this particular AP range in an earlier study as the

302   phase when the membrane resistance of the myocyte increases markedly (Figure 6B) [62]. This

303   occurs as the inward and outward currents balance each other, leading to a net whole cell current

304   that is nearly constant so that dI → 0, dV/dI → ∞ (Figure 6C), followed by a rapid reduction in

305   outward current. Figure 6D demonstrates that individual current densities have a period of inward

306   and outward current balance followed by rapid changes in I_{Kr} and other repolarizing currents at

307   *400-500 ms* time interval.

308
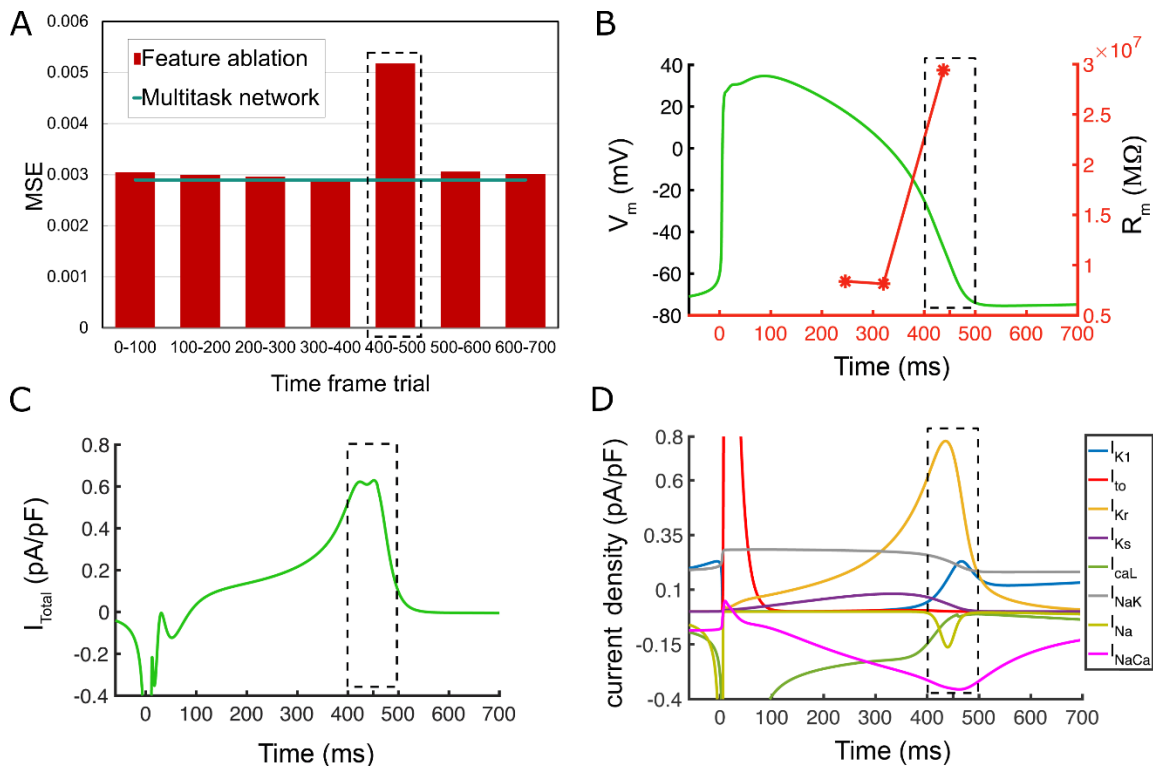
309   **Figure 6.** The feature ablation study on the proposed multitask network is performed by
310   removing iPSC-CM AP values during different time frames and evaluating their importance on
311   adult-CM AP translation. The largest effect (most important information) is observed at *400-500*
312   *ms* interval (dotted black line). (A) Comparison between intact multitask network MSE (cyan line)
313   and obtained MSE values for adult-CM AP translation during removal of indicated time frames
314   within iPSC-CM APs (red bars). (B) AP trace (green) and membrane resistance (red) as a function
315   of simulation time indicating very high values (as dI → 0, dV/dI → ∞) for the latter at *400-500*

17

316   *ms*. (C) Total current density, I$_{total}$, demonstrates a plateau followed by a rapid decline at *400-500*

317   *ms*. (D) Individual current densities indicate a period of inward and outward current balance

318   followed by rapid changes in I_{Kr} and other repolarizing components at *400-500 ms* time interval.

319

320   We next set out to demonstrate the real-world utility of the multitask classification and translation

321   network by applying the network to experimental data. We used experimental iPSC-CM APs from

322   the Kurokawa lab (Figure 7A) as the input data into the multitask network and translated to

323   predicted adult-CM APs as shown in Figure 7B. The translation notably resulted in a reduction in

324   variability in APD in the adult translated cells, consistent with our simulated results and with

325   previous experimental observations [18, 63]. In an additional validation of the multitask network,

326   we undertook a test of the network to accurately translate drug block in iPSC-CMs to adult AP

327   effects and then compared the predicted results with measured experimental data [53]. We first

328   simulated iPSC-CM APs with *50%* block of I_{Kr}. We then used these simulated APs as an input for

329   the multitask network and used the output from the translation task to predict *50%* block on adult-

330   CMs. In Figure 7C, the translated drugged APD$_{90}$ values are shown as turquoise asterisks plotted

331   against simulations from O'Hara-Rudy adult-CM APs with *50%* I_{Kr} block (red curve) and

332   experimental *50%* block of I_{Kr} by *1μM* E-4031 (blue squares) [53]. These data validate that the

333   effects of drug block in iPSC-CMs can be successfully translated to predict its effect on adult human

334   cardiomyocyte APs.

335

336
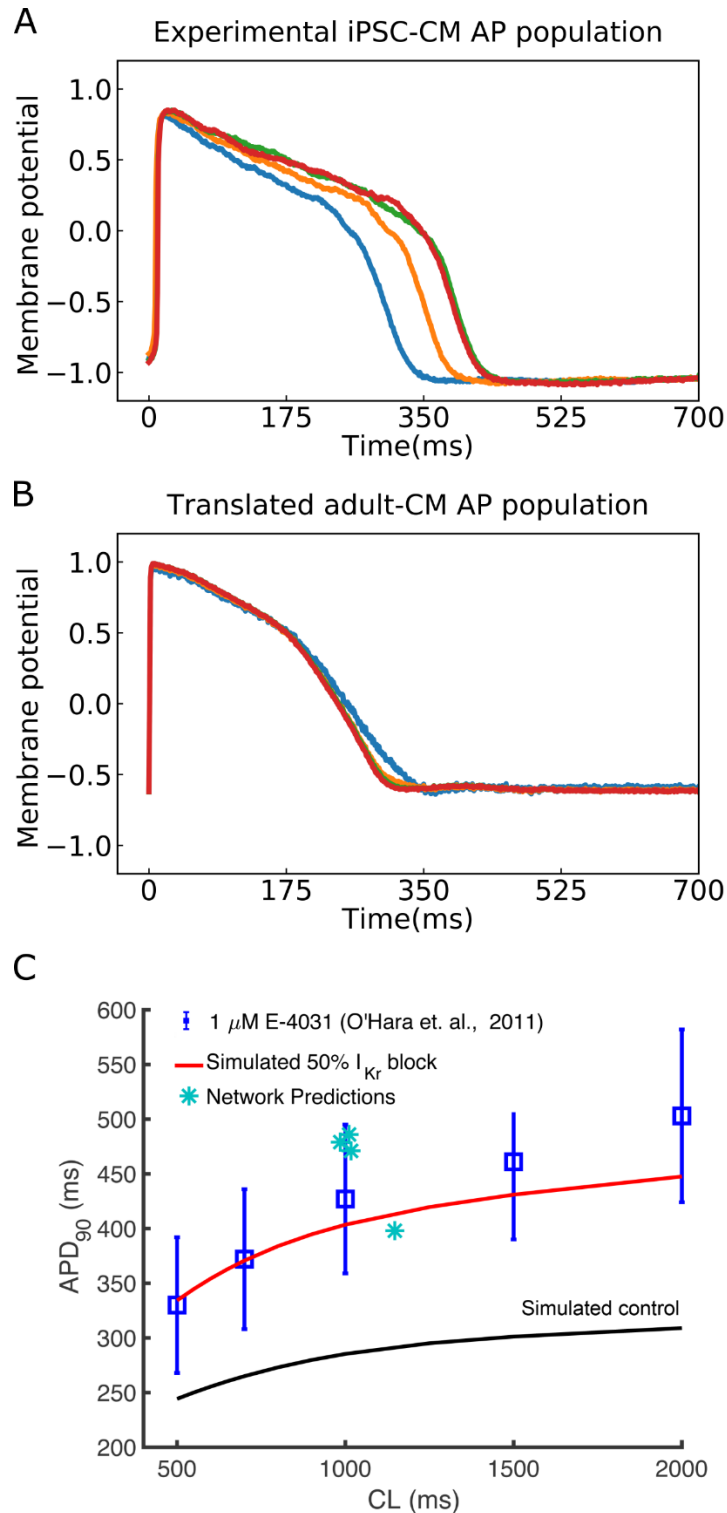
Figure 7. Translation of experimentally recorded iPSC-CM APs into adult-CM APs to validate the multitask network performance. (A) Experimentally recorded iPSC-CM APs from the Kurokawa lab. (B) Translated adult-CM APs from experimentally recorded iPSC-CM APs via the multitask network. (C) Comparing translated adult-CM APD_{90} values with *50% I_{Kr}* block (turquoise asterisks)

341   with previously published simulated (red curve for drugged and black for drug-free control) and

342   experimental (blue squares) values from O'Hara-Rudy study [1] indicates model validation.

343

Discussion

345   In this study, we developed a data-driven deep learning approach to address well known

346   shortcomings in the induced pluripotent stem cell-derived cardiomyocyte (iPSC-CM) platform. A

347   concern with iPSC-CM is that the data collection results in measurements from immature action

348   potentials, and it is unclear if these data reliably indicate impact in the adult cardiac environment

349   [14, 64-68]. Here, we set out to demonstrate a new way to allow translation of results from the

350   iPSC-CM to a mature adult cardiac response. The deep learning network also revealed new

351   mechanisms that are critical to convert iPSC-CM APs to mature adult cardiac APs.

352

353   Application of a deep learning artificial neural network to simultaneously translate and classify

354   signals from simulated iPSC-CMs for both drug-free and drugged conditions has several key

355   advantages. Because there is no need for the multitask network user to *a priori* define the

356   important system parameters, the approach is by definition an unbiased model. A key part of the

357   "artificial intelligence" is learning from the data to make decisions about which elements of the

358   data are the most important. Another benefit is the model-agnostic approach in that the learning

359   network is indifferent to the underlying form of the models and can readily translate time series

360   data from any source. The non-linearity of the system is accepted by the deep learning approach,

361   and there are no assumptions made about cardiac protein expression levels and changes in their

362   function during cardiomyocyte maturation. The deep learning artificial neural network can

363   successfully translate simple pore block and complex conformation state-dependent channel –

364   drug interaction models. The network can learn from multiple sources of data even when they are

365   generated from different models and learns from all the data sources concurrently for robust and

366   successful translation. All of these aspects of the technology presented here suggest broad

367   applicability for use across ages, species and conditions and we demonstrate its utility for

368   translating and predicting experimental data.

369

20

370   The multitask network presented here performed well in the setting of the noted variability in

371   measurements from iPSC-CM APs. As described in Figure 1, we utilized a modeling and simulation

372   approach from our recent study [52, 69] to generate a population of iPSC-CM action potentials

373   that incorporate variability comparable to that in experimental measurements. Utilizing simulated

374   data presented a unique opportunity: We were able to generate large amounts of data that were

375   used both to train and optimize the network and then to test the network with specifically

376   designated distinct simulated data sets. Utilizing simulated data to train a deep learning network

377   may constitute a widely applicable approach that could be used to train variety of networks to

378   perform multiple functions where access to comparable experimental data is not feasible.

379

380   The multitask network exhibits high accuracy in performing translation, despite large variability in

381   APDs and regardless of the underlying model form (Figure 5 and Table 1). The network was able

382   to translate iPSC-CM APs into adult-CM APs with less than *0.003* mean-squared error (MSE), *0.99*

383   R^2_score and less than *4%* error in APD_{90} prediction for both the training and test dataset. To

384   evaluate the network performance for the classification task we compared the AUROC, prediction

385   accuracy, recall and precision for both training and test datasets. The multitask network proved to

386   perform well in categorizing iPSC-CM APs into drug-free and drugged waveforms with

387   approximately *90%* accuracy (Table 1). Finally, we performed a type of network component

388   dissection by sequentially eliminated individual LSTM layers or the classification task to determine

389   if all elements of the network are important to the overall performance. The impact of removing

390   these elements of the network on its performance is shown in Table 1. The studies show that the

391   multi-task network conferred additional benefit over considering the translation task alone. For

392   example, we noted that adding the classification task to distinguish drug-free and drugged action

393   potentials could improve the performance of the translation task (Table 1).

394

395   When we performed an ablation study to prevent the deep learning network from using

396   information within prespecified time windows, the results revealed that the most important

397   information needed to predict adult-CM APs from iPSC-CM AP signals is contained in the phase of

398   the AP between 400 and 500 ms (Figure 6). This result suggests that the most important

399 information needed to distinguish iPSC-CM AP signals from adult-CM AP signals is contained in the

400 range of the AP that corresponds to a phase of exquisite sensitivity to perturbation. We have

401 identified this particular AP range in an earlier study as the phase when the membrane resistance

402 of the myocyte increases markedly (Figure 6B) [62].This occurs as the inward and outward currents

403 balance each other, leading to a net whole cell current that is unchanging (dI $\rightarrow$ 0, dV/dI $\rightarrow$ ∞),

404 followed by a rapid reduction in the outward current (Figure 6C and D).

405

406 Following the optimization and demonstration of the network as an accurate tool for both

407 translating and classifying data, we then used the same network to translate experimentally

408 obtained data. We showed that the proposed network can effectively take experimental data as

409 an input from immature iPSC-CM APs and translate those data to produce adult action potential

410 waveforms. It is notable that the variation observed in the adult-CM AP duration is smaller

411 compared to iPSC-CM APDs (Figure 7A-B). This has been observed both experimentally [18, 63]

412 and in our simulated cell environment [52, 69] . Although the simulated iPSC-CM has a large initial

413 calcium current (Figure 1C) compared to the simulated adult-CM (Figure 1D), the amplitude of

414 currents flowing through adult-CM action potential plateau is notably larger. The immature iPSC-

415 CM cells have low conductance during the AP plateau rendering it comparably higher resistance.

416 For this reason, small perturbations to the iPSC-CM APs have a larger impact on the resulting AP

417 duration than observed in adult cells [62]. We also used simulated iPSC-CM APs subject to *50%*

418 block of I_{Kr}. We translated those data to adult-CM APs and then compared with the previously

419 reported impact of *50% I_{Kr}* block on adult human cell APs from experiments [53] and noted

420 excellent agreement thereby providing validation of our network.

421

422 In this study, we show that a deep learning network can be applied to classify cells into the drug-

423 free and drugged categories and can be used to predict the impact of electrophysiological

424 perturbation across the continuum of aging from the immature iPSC-CM action potential to the

425 adult ventricular myocyte action potential. We translated experimental immature APs into mature

426 APs using the proposed network and validated the output of some key model simulations with

427 experimental data. The multitask network in this study was used for translation of iPSC-CMs to

22

428   adult APs but could be readily extended and applied to translate data across species and classify

429   data from a variety of systems. Also, another extension of the technology presented here is to

430   predict the impact of naturally occurring mutations and other genetic variations [70].

431

432   **Methods**

433

434   **Simulated data for training and testing the multitask network:**

435   *The drug-free iPSC-CM and adult-CM action potentials*

436   The Kernik *in silico* iPSC-CM baseline cells were paced from resting steady-state. The O'Hara-Rudy

437   *in silico* endocardial cell model was used for the baseline adult-CMs [53]. The control adult-CMs

438   were paced at the cycle length of *982 ms* to match the cycle length of the last beat of the

439   spontaneously depolarizing iPSC-CM AP. The iPSC-CM AP populations (n =208) were generated by

440   incorporating physiological noise (see **Simulated physiological noise currents** section below). The

441   adult-CMs were paced with noise for *100* beats after reaching steady state at the matching cycle

442   length of the last beat of iPSC-CM AP populations. The numerical method used for updating the

443   voltage was Forward Euler method [71].

444

445   *A simple drug-induced 1-50% I_{Kr} block model through G_{Kr} reduction*

446   The iPSC-CMs and the adult-CMs populations were paced with 1-50% I_{Kr} block with 1% increments.

447   This was accomplished by scaling down hERG channel (I_{Kr}) conduction, G_{Kr} , by the fraction of the

448   block, $G_{Krscale}$, in the 0.50 − 0.99 range with 0.01 decrements (see central rows in Fig. 1G). The

449   adult-CM model was simulated at five varying beating rates for each percentage of block that

450   matches to the last beat of iPSC-CMs with *1-50% I_{Kr}* block (n = 250). For example, one drugged

451   adult-CM (*50% I_{Kr}* inhibition) was paced at cycle length of *1047 ms* to match the cycle length of

452   the last beat of iPSC-CMs AP with *50% I_{Kr}* block.

453

454   *Complex model of conformation-state dependent I_{Kr} block in the presence of 2.72 ng/mL dofetilide*

455   The I_{Kr} channel Hodgkin-Huxley model in both iPSC-CM and adult-CM AP models was replaced with

456   a drug − hERG channel interaction Markov model (see bottom rows in Fig. 1G) that we have

457 previously published [72]. iPSC-CM (n = 300) and adult-CM AP populations (n = 300) were

458 generated with physiological noise in the presence of *2.72 ng/mL* dofetilide, a potent hERG

459 channel blocker. The adult-CM populations were paced with dofetilide for 100 beats after

460 reaching steady state at the matching cycle length of the last beat of iPSC-CM AP populations with

461 dofetilide as described above.

462 **Simulated physiological noise currents:**

463 Simulated noise current was added to the last 100 paced beats in the simulated AP models, and

464 simulated APs were recorded at the 2000th paced beat in single cells. This noise current was

465 modeled using the equation from [55],

466 $$V_{t+\Delta t} = V_t - \frac{I(V_t)\Delta t}{C_m} + \xi n \sqrt{\Delta t} \qquad (1)$$

467 Where $n \in N(0,1)$ is a random number from a Gaussian distribution, and Δt is the time step. $\xi = 0.3$

468 is the diffusion coefficient, which is the amplitude of noise. The noise current was generated and

469 applied to membrane potential, V_t, throughout the last 100 beats of simulated time course.

470

471 **Experimental iPSC-CMs:**

472 Human iPSC-CMs (201B7, RIKEN BRC, Tsukuba, Japan) were cultured and subcultured on *SNL76/7*

473 feeder cells as described in detail previously [73]. Cardiomyocyte differentiation was performed

474 as described [73]. Commercially available iCell-cardiomyocytes (FUJIFILM Cellular Dynamics, Inc.,

475 Tokyo, Japan) were cultured according to the manual provided from the company. Action

476 potentials were recorded with the perforated configuration of the patch-clamp technique as

477 described in detail previously [73]. Measurements were performed at *36 ± 1 °C* with the external

478 solution composed of (in *mM*): *NaCl* (*135*), *NaH$_2$PO$_4$* (*0.33*), *KCl* (*5.4*), *CaCl$_2$* (*1.8*), *MgCl$_2$* (*0.53*),

479 glucose (*5.5*), *HEPES*, *pH 7.4*. To achieve patch perforation (*10-20 MΩ*; series resistances),

480 amphotericin B (*0.3-0.6 µg/mL*) was added to the internal solution composed of (in *mM*): aspartic

481 acid (*110*), *KCl* (30), *CaCl$_2$* (*1*), adenosine-5′-triphosphate magnesium salt (*5*), creatine phosphate

482 disodium salt (*5*), *HEPES* (*5*), *EGTA* (*11*), *pH 7.25*. In quiescent cardiomyocytes, action potentials

483 were elicited by passing depolarizing current pulses (*2 ms* in duration) of suprathreshold intensity

484 (*120 %* of the minimum input to elicit action potentials) with a frequency at *1 Hz* unless noted

485 otherwise.

24

486   **The multitask network architecture:**

487   The multitask network was comprised of two stacked LSTM layers followed by independent fully

488   connected layers (Figure 3A) for the classification and translation tasks.   The LSTM layers

489   memorized the important information the network needed to perform two discussed tasks and

490   then transferred the extracted information (features) into the subsequent fully connected layers

491   to translate iPSC-CM APs into adult-CM AP waveforms (Figure 3B) and classify iPSC-CM APs into

492   drug-free and drugged categories (Figure 3C).

493

494   *Long-short term memory (LSTM) layers (Figure 3D):*

495   We used LSTM layers as the first two layers of the multitask network to promote network temporal

496   information learning which data in a sequence was important to keep or to throw away. At each

497   time step, the LSTM cell took in three different pieces of information, the current input data

498   (AP_{iPSC_t}), incoming short-term memory (hidden state) (h_{t-1}) and incoming long-term memory

499   (cell state) (C_{t-1}). The LSTM layers were responsible for extracting the most important

500   information while scanning the AP traces using the short- and long-term memory components.

501   The short-term memory weighted the importance of AP values at subsequent time steps and long-

502   term memory has been using the short-term memory to decide the overall importance of all AP

503   values from the beginning (t = 0 ms) to the end (t = 701 ms) for performing classification and

504   translation tasks. The LSTM cells contained internal mechanisms called gates.   The gates were

505   neural network with weights (*w*) and bias terms (*b*) that regulated the flow of information at each

506   time step before passing on the long-term and short-term information to the next cell [74]. These

507   gates are called input gate, forget gate, and output gate (Figure 3D).

508

509   The forget gate, as the name implies, determined which information from the long-term memory

510   should be kept or discarded. This was done by multiplying the incoming long-term memory by a

511   forget vector generated by the current input (AP_{iPSC_t}) and incoming short-term memory (h_{t-1}).

512   To obtain the forget vector, the incoming short-term memory and current input were passed

513   through a sigmoid function (σ_f) [75]. The output vector of sigmoid function, F_t, (Eq. 2) was a binary

514 comprising 0s and 1s and was then multiplied by the incoming long-term memory (C_{t-1}). to

515 choose, which parts of the long-term memory were retained.

516 $$F_t = \sigma_f\left(w_f AP_{iPSC_t} + w_f h_{t-1} + b_f\right) \quad t \in \{0,1,\dots,701\} \tag{2}$$

517 The input gate decided what new information is being stored in current long-term memory (C_t).

518 It considered the current input (AP_{iPSC_t}) and the incoming short-term memory (h_{t-1}) and

519 transformed the values to be between 0 (unimportant) and 1 (important) using a sigmoid

520 activation function (σ_i) (Eq. 3). The second layer in input gate took the incoming short-term

521 memory (h_{t-1}) and current input (AP_{iPSC_t}) and passed them through a hyperbolic tangent

522 activation function ($tanh_i$) to regulate the network computation (Eq. 4).

523 $$I_t = \sigma_i\left(W_i AP_{iPSC_t} + W_i h_{t-1} + b_i\right) \quad t \in \{0,1,\dots,701\} \tag{3}$$

524 $$S_t = tanh_i\left(w_s AP_{iPSC_t} + w_s h_{t-1} + b_s\right) \tag{4}$$

525 The outputs from the forget and input gates then underwent a pointwise addition to find the

526 current long-term memory (C_t) (Eq . 5), which was then passed on to the next cell.

527 $$C_t = F_t * C_{t-1} + I_t * S_t \tag{5}$$

528 Finally, the output gate utilized current input (AP_{iPSC_t}) and the incoming short-term memory

529 (h_{t-1}) and passed them into a sigmoid function (σ_o) (Eq. 6). Then the current long-term memory

530 (C_t) passed through a *tanh* activation function ($tanh_o$) and the outputs from these two processes

531 were multiplied to produce the current short-term memory h_t (Eq. 7).

532 $$O_t = \sigma_o\left(w_o AP_{iPSC_t} + w_o h_{t-1} + b_o\right) \tag{6}$$

533 $$h_t = O_t * tanh_o(C_t) \tag{7}$$

534 The short-term and long-term memory produced by these gates were carried over to the next cell

535 for the process to be repeated. The output of LSTM layers for each time step (h_t) was obtained

536 from the short-term memory, also known as the hidden state, and was subsequently passed into

537 fully connected layers to perform the translation and classification tasks as described below.

538

539

540   *Fully connected layers (Figure 3E):*

541   The fully connected neural network layers contained input, hidden and output layers (Figure 2E)

542   with various numbers of neurons (l_r). Every neuron in a layer was connected to neurons in the

543   next layer [76]. Fully connected layers received the output of LSTM layers as input. The fully

544   connected layers calculated a weighted sum of LSTM outputs and added a bias term to the

545   outputs. These data were then passed to an activation function (f) to define the output for each

546   neuron (Eqs. 8 and 9)   [77].

547    $a_j^k = f(Z_j^k)$ (8)

548    $Z_j^k = W_{i,j}^k * a_j^{k-1} + b^k$ (9)

549   Where $k \in \{1, \ldots, n\}$ and (i , j) represent the number of hidden layers and neurons in each pair of

550   subsequent hidden layers (l_r, l_{r+1}). The optimized values for these parameters were found via

551   hyperparameter tunning where, a^k is each neuron output where $a^0 \in \{h_1, \ldots, h_m\}$ is the LSTM

552   layers output and the input to the fully connected layers and a^{n+1} is the network output:

553    $\hat{y} \epsilon \{y_{t_i}, y_{c_i}\}$ where y_{t_i} and y_{c_i} are the outputs for translation and classification tasks, respectively.

554   We first assigned random values to all network parameters θ_t; each neuron weight $(W_{i,j})$ (Figure

555   3E), bias term (b) which is a constant added to calculate the neurons output and other network

556   hyperparameters (the number of hidden layers, the number of neurons for each hidden layer and

557   activation functions for each hidden layer) to start the optimization process for finding the best

558   network infrastructure. Next, we estimated the network errors using mean squared error, MSE

559   (Eq. 10) and cross-entropy loss functions (Eq. 11) to map the translation and classification tasks

560   [54, 78], respectively.

561    $MSE = \frac{1}{m} \sum_{i=1}^{n} \|y_{t_i} - \hat{y}_{t_i}\|^2$ (10)

562    $CrossEntropy = -\left(y_{c_i} \log(\hat{y}_{c_i}) + (1 - y_{c_i})\log(1 - \hat{y}_{c_i})\right)$ (11)

563   where m is the total number of LSTM layers outputs (h_m) and y_{t_i} and $\hat{y}_{t_i}$ are the simulated and

564   translated adult-CM APs (the network output for translation task). The y_{c_i} is binary indicator of

565   class labels for iPSC-CM APs (0 for drug-free or 1 for drugged categories) and $\hat{y}_{c_i}$ is predicted

566   probability of APs being classified into the discussed classes. We used sum of both loss functions

567   (Eq. 12) to calculate the overall network error (J) for both translation and classification tasks during

27

568 the network training process. We updated network parameters (θ_{t+1}) using adaptive momentum

569 estimation (ADAM) optimization algorithm [79] based on the average gradient of overall loss

570 function with respect to the network parameters for 64 randomly selected simulated AP traces

571 (mini-batch = 64) at each training iteration (Eqs. 13-15).

572 $$J(\theta_t) = CrossEntropy_{Classification}(\theta_t) + \text{MSE}_{Translation}(\theta_t) \tag{12}$$

573 $$\theta_{t+1} = \theta_t - \frac{\alpha \cdot \widehat{m}_t}{\sqrt{\widehat{v}_t} + \epsilon} \quad , \qquad \theta_t \, \epsilon \, \{W_{i,j}^n, b_j^{\,n}\} \tag{13}$$

574 $$\widehat{m}_t = \frac{m_t}{1 - \beta_1}, \quad \text{where} \quad m_t = (1 - \beta_1)\nabla J(\theta_t) + \beta_1 m_{t-1} \tag{14}$$

575 $$\widehat{v}_t = \frac{v_t}{1 - \beta_2}, \quad \text{where} \quad v_t = (1 - \beta_2)\big(\nabla J(\theta_t)\big)^2 + \beta_2 v_{t-1} \tag{15}$$

576

577 We used a rectified linear unit (ReLu) [80] as activation function in Eq. 8 to calculate the output

578 for each hidden layer neuron at each training iteration. We used dropout regularization [81] to

579 randomly drop neurons with 0.2 probability of elimination along with their connections from the

580 LSTM and fully connected layers during training to reduce the overfitting. We kept updating the

581 network parameters using ADAM optimization algorithm (Eq. 13) to find global minimum of loss

582 function (Eq. 12). We computed the exponential average of the gradient (Eq. 14) as well as the

583 square of the gradient (Eq. 15) for each parameter (θ_t) where α is the learning rate equal to 0.001,

584 β_1, β_2 are first and second momentum coefficients equal to *0.9* and *0.999*, and ϵ is a small term

585 equal to *1e-8* preventing division by zero.

586

Computational workflow (Figure 4)

588 We first preprocessed iPSC-CM and adult-CM APs by applying a digital forward and backward data

589 filtering technique [56] and normalizing the AP values for more efficient training process. Next, we

590 split the preprocessed data in 70:10:20 ratio into training, validation and test data sets,

591 respectively, and implemented the network architecture using Pytorch [82]. During the training

592 process the multitask network received iPSC-CM AP time course data as inputs and predicted

593 adult-CM AP time courses. The network also received the category (drug-free and drugged) of the

594 iPSC-CM AP data. The network next calculated the MSE (Eq. 10) between predicted AP waveforms

595 and the expected waveforms for adult-CM APs. It also calculated cross-entropy (Eq. 11) between

596 the predicted category for the iPSC-CM AP and the expected value. The cross-entropy was added

597   to the calculated MSE to determine the total loss for training. The ADAM optimization algorithm

598   was then used to update the network weights and bias terms.

599

600   We performed updating the network parameters (Eq. 13) and monitored the network

601   performance for the training and validation data sets until the point at which the network

602   performance on the training data set began to degrade compared to the validation dataset. This

603   process was used to identify the optimal number of iterations (epochs = 300) for the training

604   process. The last trained network was designated as the best possible model to perform both

605   translation and classification tasks. We then used a holdout test dataset and calculated MSE (Eq.

606   10), R^2_score (Eqs. 16-17 below) and the error in prediction for adult-CM APD_{90} as evaluation

607   metrics to assess the performance of the network for translation task and the area under the

608   receiver operating characteristic (AUROC) curve, accuracy, recall and precision to measure

609   capability of network for classification task as described below. The network codes have been

610   made   publicly   available   at   Clancy   lab   Github.

611   (https://github.com/ClancyLabUCD/Multitask_network)

612

Evaluation metrics for the translation and classification tasks

614   As we discussed, we used MSE and cross-entropy loss functions for performance evaluation of

615   translation and classification tasks. In addition to MSE, we computed R^2_score [57] (Eqs. 16,17) to

616   measure how close the translated adult-CM AP $(\hat{y}_{t_i})$ was to the expected simulated adult-CM AP

617   (y_{t_i}). We compared the histogram distribution of simulated and translated adult-CM APD_{90} values

618   and the error in APD_{90} prediction to assess the accuracy of network prediction.

619    $$\bar{\hat{y}}_{t_i} = \frac{1}{m}\sum_{i=1}^{m}\hat{y}_{t_i} \tag{16}$$

620    $$R^2 = \frac{\Sigma_i(\hat{y}_{t_i} - \bar{\hat{y}}_{t_i})}{\Sigma_i\left(y_{t_i} - \bar{y}_{t_i}\right)} \tag{17}$$

621

622   We used AUROC to measure the capability of the model to distinguish between drug-free and

623   drugged iPSC-CM APs [58]. AUROC is the area under the Receiver Operating Characteristic (ROC)

624   curve, which is a plot of the false positive rate (FPR), the probability that the network classified

29

625   drug-free iPSC-CM APs into drugged categories (FP) (Eq. 18) versus the true positive rate (TPR) or

626   recall, the probability that the network correctly classified drugged iPSC-CM APs into drugged

627   category (TP) (Eq. 19). AUROC close to 1 indicated a model with a desirable measure of

628   separability, while a poor model had AUROC near 0, which means that it had poor separability.

629

630   In addition, we used recall, accuracy, and precision to describe the performance of the network

631   for the classification task [13], where the accuracy and precision indicated the proportion of all

632   correct, TP + true negatives (TN), i.e., predicted drug-free APs (Eq. 20) and correct positive

633   identifications (Eq. 21). False negatives (FN) in Eqs. 19-20 were the total number of drugged iPSC-

634   CM APs classified as drug-free.

635      $\text{FPR} = \frac{FP}{FP+TN}$ (18)

636      $\text{Recall} = \frac{TP}{TP+FN}$ (19)

637      $\text{Accuracy} = 100 * \frac{TP + TN}{TP+TN+FP+FN}$ (20)

638      $Precision = \frac{TP}{TP+FP}$ (21)

639

640

641   **References**

642

643   1.   Shaheen, N., et al., *Human induced pluripotent stem cell-derived cardiac cell sheets*
644   *expressing genetically encoded voltage indicator for pharmacological and arrhythmia*
645   *studies.* Stem cell reports, 2018. **10**(6): p. 1879-1894.
646   https://doi.org/10.1016/j.stemcr.2018.04.006
647   2.   Leyton-Mange, J.S., et al., *Rapid cellular phenotyping of human pluripotent stem cell-*
648   *derived cardiomyocytes using a genetically encoded fluorescent voltage sensor.* Stem cell
649   reports, 2014. **2**(2): p. 163-170. https://doi.org/10.1016/j.stemcr.2014.01.003
650   3.   Sun, N., et al., *Patient-specific induced pluripotent stem cells as a model for familial*
651   *dilated cardiomyopathy.* Sci Transl Med, 2012. **4**(130): p. 130ra47.
652   https://doi.org/10.1126/scitranslmed.3003552
653   4.   Lan, F., et al., *Abnormal calcium handling properties underlie familial hypertrophic*
654   *cardiomyopathy pathology in patient-specific induced pluripotent stem cells.* Cell Stem
655   Cell, 2013. **12**(1): p. 101-13. https://doi.org/10.1016/j.stem.2012.10.010
656   5.   Burridge, P.W., et al., *Human induced pluripotent stem cell-derived cardiomyocytes*
657   *recapitulate the predilection of breast cancer patients to doxorubicin-induced*
658   *cardiotoxicity.* Nat Med, 2016. **22**(5): p. 547-56. https://doi.org/10.1038/nm.4087

6. Doss, M.X. and A. Sachinidis, *Current challenges of iPSC-based disease modeling and therapeutic implications.* Cells, 2019. **8**(5): p. 403. https://doi.org/10.3390/cells8050403

7. Collins, T.A., M.G. Rolf, and A. Pointon, *Current and future approaches to nonclinical cardiovascular safety assessment.* Drug Discovery Today, 2020. https://doi.org/10.1016/j.drudis.2020.03.011

8. Wu, J.C., et al., *Towards precision medicine with human iPSCs for cardiac channelopathies.* Circulation research, 2019. **125**(6): p. 653-658. https://doi.org/10.1161/CIRCRESAHA.119.315209

9. Sayed, N., C. Liu, and J.C. Wu, *Translation of human-induced pluripotent stem cells: from clinical trial in a dish to precision medicine.* Journal of the American College of Cardiology, 2016. **67**(18): p. 2161-2176. http://dx.doi.org/10.1016/j.jacc.2016.01.083

10. Matsa, E., J.H. Ahrens, and J.C. Wu, *Human induced pluripotent stem cells as a platform for personalized and precision cardiovascular medicine.* Physiological Reviews, 2016. **96**(3): p. 1093-1126. https://doi.org/10.1152/physrev.00036.2015

11. Tveito, A., et al., *Inversion and computational maturation of drug response using human stem cell derived cardiomyocytes in microphysiological systems.* Scientific reports, 2018. **8**(1): p. 1-14. https://doi.org/10.1038/s41598-018-35858-7

12. Tveito, A., et al., *Computational translation of drug effects from animal experiments to human ventricular myocytes.* Scientific Reports, 2020. **10**(1): p. 1-11. https://doi.org/10.1038/s41598-020-66910-0

13. Sube, R. and E.A. Ertel, *Cardiomyocytes Derived from Human Induced Pluripotent Stem Cells: An In-Vitro Model to Predict Cardiac Effects of Drugs.* Journal of Biomedical Science and Engineering, 2017. **10**(11): p. 527. https://doi.org/10.4236/jbise.2017.1011040

14. Navarrete, E.G., et al., *Screening drug-induced arrhythmia using human induced pluripotent stem cell–derived cardiomyocytes and low-impedance microelectrode arrays.* Circulation, 2013. **128**(11_suppl_1): p. S3-S13. https://doi.org/10.1161/CIRCULATIONAHA.112.000570

15. Lieu, D.K., et al., *Mechanism-based facilitated maturation of human pluripotent stem cell-derived cardiomyocytes.* Circ Arrhythm Electrophysiol, 2013. **6**(1): p. 191-201. https://doi.org/10.1161/CIRCEP.111.973420

16. Veerman, C.C., et al., *Immaturity of human stem-cell-derived cardiomyocytes in culture: fatal flaw or soluble problem?* Stem Cells Dev, 2015. **24**(9): p. 1035-52. https://doi.org/10.1089/scd.2014.0533

17. Tu, C., B.S. Chao, and J.C. Wu, *Strategies for Improving the Maturity of Human Induced Pluripotent Stem Cell-Derived Cardiomyocytes.* Circ Res, 2018. **123**(5): p. 512-514. https://doi.org/10.1161/CIRCRESAHA.118.313472

18. Blinova, K., et al., *International multisite study of human-induced pluripotent stem cell-derived cardiomyocytes for drug proarrhythmic potential assessment.* Cell reports, 2018. **24**(13): p. 3582-3592. https://doi.org/10.1016/j.celrep.2018.08.079

19. Sala, L., M. Bellin, and C.L. Mummery, *Integrating cardiomyocytes from human pluripotent stem cells in safety pharmacology: has the time come?* British journal of pharmacology, 2017. **174**(21): p. 3749-3765. https://doi.org/10.1111/bph.13577

20. Gong, J.Q. and E.A. Sobie, *Population-based mechanistic modeling allows for quantitative predictions of drug responses across cell types.* NPJ systems biology and applications, 2018. **4**(1): p. 1-11. https://doi.org/10.1038/s41540-018-0047-2

31

21. de Korte, T., et al., *Unlocking personalized biomedicine and drug discovery with human induced pluripotent stem cell–derived Cardiomyocytes: fit for purpose or forever elusive?* Annual Review of Pharmacology and Toxicology, 2020. **60**: p. 529-551. https://doi.org/10.1146/annurev-pharmtox-010919-023309

22. Koivumäki, J.T., et al., *Structural immaturity of human iPSC-derived cardiomyocytes: in silico investigation of effects on function and disease modeling.* Frontiers in physiology, 2018. **9**: p. 80. https://doi.org/10.3389/fphys.2018.00080

23. Alhusseini, M.I., et al., *Machine Learning to Classify Intracardiac Electrical Patterns During Atrial Fibrillation: Machine Learning of Atrial Fibrillation.* Circulation: Arrhythmia and Electrophysiology, 2020. **13**(8): p. e008160. https://doi.org/10.1161/CIRCEP.119.008160

24. Rogers, A.J., et al., *Machine Learned Cellular Phenotypes Predict Outcome in Ischemic Cardiomyopathy.* Circulation Research, 2020. https://doi.org/10.1161/CIRCRESAHA.120.317345

25. Sevakula, R.K., et al., *State-of-the-Art machine learning techniques aiming to improve patient outcomes pertaining to the cardiovascular system.* Journal of the American Heart Association, 2020. **9**(4): p. e013924. https://doi.org/10.1161/JAHA.119.013924

26. Jin, Z., et al. *HeartToGo: a personalized medicine technology for cardiovascular disease prevention and detection.* in *2009 IEEE/NIH Life Science Systems and Applications Workshop.* 2009. IEEE. https://doi.org/10.1109/LISSA.2009.4906714

27. Trayanova, N.A., D.M. Popescu, and J.K. Shade, *Machine Learning in Arrhythmia and Electrophysiology.* Circulation Research, 2021. **128**(4): p. 544-566. https://doi.org/10.1161/CIRCRESAHA.120.317872

28. Hochreiter, S. and J. Schmidhuber, *Long short-term memory.* Neural computation, 1997. **9**(8): p. 1735-1780. https://doi.org/10.1162/neco.1997.9.8.1735

29. Guo, A., et al., *Predicting cardiovascular health trajectories in time-series electronic health records with LSTM models.* BMC Medical Informatics and Decision Making, 2021. **21**(1): p. 1-10. https://doi.org/10.1186/s12911-020-01345-1

30. Shi, K., et al., *Contactless analysis of heart rate variability during cold pressor test using radar interferometry and bidirectional LSTM networks.* Scientific reports, 2021. **11**(1): p. 1-13. https://doi.org/10.1038/s41598-021-81101-1

31. Picon, A., et al., *Mixed convolutional and long short-term memory network for the detection of lethal ventricular arrhythmia.* PloS one, 2019. **14**(5): p. e0216756. https://doi.org/10.1371/journal.pone.0216756

32. Ballinger, B., et al. *DeepHeart: semi-supervised sequence learning for cardiovascular risk prediction.* in *Thirty-Second AAAI Conference on Artificial Intelligence.* 2018.

33. He, R., et al., *Automatic cardiac arrhythmia classification using combination of deep residual network and bidirectional LSTM.* IEEE Access, 2019. **7**: p. 102119-102135. https://doi.org/10.1109/ACCESS.2019.2931500

34. Hou, B., et al., *LSTM Based Auto-Encoder Model for ECG Arrhythmias Classification.* IEEE Transactions on Instrumentation and Measurement, 2019. https://doi.org/10.1109/TIM.2019.2910342

35. Warrick, P. and M.N. Homsi. *Cardiac arrhythmia detection from ECG combining convolutional and long short-term memory networks.* in *2017 Computing in Cardiology (CinC).* 2017. IEEE. https://doi.org/10.22489/CinC.2017.161-460

750 36. Oh, S.L., et al., *Automated diagnosis of arrhythmia using combination of CNN and LSTM*
751   *techniques with variable length heart beats.* Computers in biology and medicine, 2018.
752   **102**: p. 278-287. https://doi.org/10.1016/j.compbiomed.2018.06.002
753 37. Chen, C., et al., *Automated arrhythmia classification based on a combination network of*
754   *CNN and LSTM.* Biomedical Signal Processing and Control, 2020. **57**: p. 101819.
755   https://doi.org/10.1016/j.bspc.2019.101819
756 38. Wang, L. and X. Zhou, *Detection of congestive heart failure based on LSTM-based deep*
757   *network via short-term RR intervals.* Sensors, 2019. **19**(7): p. 1502.
758   https://doi.org/10.3390/s19071502
759 39. Bian, M., et al. *An accurate lstm based video heart rate estimation method.* in *Chinese*
760   *Conference on Pattern Recognition and Computer Vision (PRCV).* 2019. Springer.
761   https://doi.org/10.1007/978-3-030-31726-3_35
762 40. Maragatham, G. and S. Devi, *LSTM model for prediction of heart failure in big data.*
763   Journal of medical systems, 2019. **43**(5): p. 1-13. https://doi.org/10.1007/s10916-019-
764   1243-3
765 41. Yildirim, O., et al., *A new approach for arrhythmia classification using deep coded*
766   *features and LSTM networks.* Computer methods and programs in biomedicine, 2019.
767   **176**: p. 121-133. https://doi.org/10.1016/j.cmpb.2019.05.004
768 42. Wang, E.K., X. Zhang, and L. Pan, *Automatic classification of CAD ECG signals with*
769   *SDAE and bidirectional long short-term network.* IEEE Access, 2019. **7**: p. 182873-
770   182880. https://doi.org/10.1109/ACCESS.2019.2936525
771 43. Martis, R.J., et al., *Application of higher order cumulant features for cardiac health*
772   *diagnosis using ECG signals.* International journal of neural systems, 2013. **23**(04): p.
773   1350014. https://doi.org/10.1142/S0129065713500147
774 44. Liu, F., et al. *A LSTM and CNN based assemble neural network framework for*
775   *arrhythmias classification.* in *ICASSP 2019-2019 IEEE International Conference on*
776   *Acoustics, Speech and Signal Processing (ICASSP).* 2019. IEEE.
777   https://doi.org/10.1109/ICASSP.2019.8682299
778 45. Yildirim, Ö., *A novel wavelet sequence based on deep bidirectional LSTM network model*
779   *for ECG signal classification.* Computers in biology and medicine, 2018. **96**: p. 189-202.
780   https://doi.org/10.1016/j.compbiomed.2018.03.016
781 46. Yang, P.-C., et al., *A computational pipeline to predict cardiotoxicity: From the atom to*
782   *the rhythm.* Circulation research, 2020. **126**(8): p. 947-964.
783   https://doi.org/10.1161/CIRCRESAHA.119.316404
784 47. Cai, C., et al., *Deep learning-based prediction of drug-induced cardiotoxicity.* Journal of
785   chemical information and modeling, 2019. **59**(3): p. 1073-1084.
786   https://doi.org/10.1021/acs.jcim.8b00769
787 48. Zhang, Y., et al., *Prediction of hERG K+ channel blockage using deep neural networks.*
788   Chemical Biology & Drug Design, 2019. **94**(5): p. 1973-1985.
789   https://doi.org/10.1111/cbdd.13600
790 49. Dickson, C.J., C. Velez-Vega, and J.S. Duca, *Revealing molecular determinants of hERG*
791   *blocker and activator binding.* Journal of chemical information and modeling, 2019.
792   **60**(1): p. 192-203. https://doi.org/10.1021/acs.jcim.9b00773
793 50. Ryu, J.Y., et al., *DeepHIT: a deep learning framework for prediction of hERG-induced*
794   *cardiotoxicity.* Bioinformatics, 2020. **36**(10): p. 3049-3055.
795   https://doi.org/10.1093/bioinformatics/btaa075

841   67.   Sinnecker, D., et al., *Induced pluripotent stem cell-derived cardiomyocytes: a versatile*
842   *tool for arrhythmia research.* Circulation Research, 2013. **112**(6): p. 961-968.
843   https://doi.org/10.1161/CIRCRESAHA.112.268623
844   68.   Blinova, K., et al., *Comprehensive translational assessment of human-induced*
845   *pluripotent stem cell derived cardiomyocytes for evaluating drug-induced arrhythmias.*
846   Toxicological Sciences, 2017. **155**(1): p. 234-247. https://doi.org/10.1093/toxsci/kfw200
847   69.   Kernik, D.C., et al., *A computational model of induced pluripotent stem-cell derived*
848   *cardiomyocytes for high throughput risk stratification of KCNQ1 genetic variants.* PLOS
849   Computational Biology, 2020. **16**(8): p. e1008109.
850   https://doi.org/10.1371/journal.pcbi.1008109
851   70.   Yoshinaga, D., et al., *Phenotype-based high-throughput classification of long QT*
852   *syndrome subtypes using human induced pluripotent stem cells.* Stem cell reports, 2019.
853   **13**(2): p. 394-404. https://doi.org/10.1016/j.stemcr.2019.06.007
854   71.   Atkinson, K.E., *An introduction to numerical analysis.* 2008: John wiley & sons.
855   72.   Yang, P.C., et al., *A Computational Pipeline to Predict Cardiotoxicity: From the Atom to*
856   *the Rhythm.* Circ Res, 2020. **126**(8): p. 947-964.
857   https://doi.org/10.1161/CIRCRESAHA.119.316404
858   73.   Li, M., et al., *Overexpression of KCNJ2 in induced pluripotent stem cell-derived*
859   *cardiomyocytes for the assessment of QT-prolonging drugs.* Journal of Pharmacological
860   Sciences, 2017. **134**(2): p. 75-85. https://doi.org/10.1016/j.jphs.2017.05.004
861   74.   Cheng, J., L. Dong, and M. Lapata, *Long short-term memory-networks for machine*
862   *reading.* arXiv preprint arXiv:1601.06733, 2016.
863   75.   Olah, C., *Understanding LSTM Networks. Aug. 2015.* URL https://colah. github.
864   io/posts/2015-08-Understanding-LSTMs, 2017.
865   76.   Krogh, A., *What are artificial neural networks?* Nature biotechnology, 2008. **26**(2): p.
866   195-197. https://doi.org/10.1038/nbt1386
867   77.   Carugo, O., F. Eisenhaber, and Carugo, *Data mining techniques for the life sciences.* Vol.
868   609. 2010: Springer. https://doi.org/10.1007/978-1-4939-3572-7
869   78.   Murphy, K.P., *Machine learning: a probabilistic perspective.* 2012: MIT press.
870   79.   Kingma, D.P. and J. Ba, *Adam: A method for stochastic optimization.* arXiv preprint
871   arXiv:1412.6980, 2014.
872   80.   Glorot, X., A. Bordes, and Y. Bengio. *Deep sparse rectifier neural networks.* in
873   *Proceedings of the fourteenth international conference on artificial intelligence and*
874   *statistics.* 2011. JMLR Workshop and Conference Proceedings.
875   81.   Zaremba, W., I. Sutskever, and O. Vinyals, *Recurrent neural network regularization.*
876   arXiv preprint arXiv:1409.2329, 2014.
877   82.   Ketkar, N., *Introduction to pytorch*, in *Deep learning with python.* 2017, Springer. p.
878   195-208. https://doi.org/10.1007/978-1-4842-2766-4_12
879